Atomic-scale study on the dopant distribution in phosphorus and boron-doped Si nanocrystals/SiO2 multilayers

Dongke Li, Jiaming Chen, Zhaoguo Xue, Teng Sun, Junnan Han, Wanghua Chen, Etienne Talbot, Rémi Demoulin, Wei Li, Jun Xu, et al.

Atomic-scale study on the dopant distribution in phosphorus and boron-doped Si nanocrystals/SiO_2 multilayers

Dongke Li [a,b], Jiaming Chen [a], Zhaoguo Xue [c], Teng Sun [a], Junnan Han [a], Wanghua Chen [d,*], Etienne Talbot [e], Rémi Demoulin [e], Wei Li [a], Jun Xu [a,*], Kunji Chen [a]

[a] School of Electronic Science and Engineering, National Laboratory of Solid State Microstructures, Collaborative Innovation Center of Advanced Microstructures, Jiangsu Provincial Key Laboratory of Advanced Photonic and Electronic Materials, Nanjing University, Nanjing 210000, China
[b] Zhejiang Provincial Key Laboratory of Power Semiconductor Materials and Devices, ZJU-Hangzhou Global Scientific and Technological Innovation Center, School of Materials Science and Engineering, Zhejiang University, Hangzhou 311200, China
[c] Institute of Solid Mechanics, Beihang University, Beijing 100191, China
[d] School of Physical Science and Technology, Ningbo University, Ningbo 315211, China
[e] Normandie University, UNIROUEN, INSA Rouen, CNRS, Groupe de Physique des Matériaux, 76000 Rouen, France

A B S T R A C T

Understanding the distributions and behaviors of dopants in Si nanocrystal are the primary and necessary issues to realize the controllable doping at nanoscale and develop the next generation of optoelectronic devices. This work reports the atomic-scale distributions of phosphorus and boron dopants in Si nanocrystals multilayers. The phosphorus-doped and boron-doped Si nanocrystals/SiO_2 multilayers are fabricated by PECVD and subsequently annealed at 1000 °C. It is found that the locations of phosphorus are redistributed after the formation of Si nanocrystals due to the combined effects of formation energy and self-purification. Phosphorus dopants are mainly distributed at the Si nanocrystals surfaces to passivate the dangling bonds, while part of them incorporate into Si nanocrystals lattice sites to provide free electrons. However, boron dopants exhibit different distributions in contrast to phosphorus. The concentration of boron on Si nanocrystals surfaces can reach as high as 40.0 at. %, which forms a dopant-shell covering on Si nanocrystals. Meanwhile, the boron dopant-shell can modify the surface states of Si nanocrystals like Si-oxide related emission centers and dangling bonds, which is responsible for the luminescence properties. Moreover, the boron-aggregations with concentration near 74.8 at. % are appeared inside Si nanocrystals and led to the damage of crystalline lattice.

1. Introduction

Due to the size-controllable bandgap and high recombination efficiency under the quantum confinement effect, Si nanocrystal (Si NC) is regarded as one of the most promising candidates of Si-based optical materials [1–3]. The related applications in the new generation of optoelectronic devices, like LED [4], all Si-based tandem solar cells [5] and neuromorphic computing [6] are also gradually reported. Recently, phosphorus (P) and/or boron (B) doping in Si NCs are believed as important methods to further develop novel optoelectronic properties and have attracted extensive attentions [7–10]. However, achieving the effective doping in Si NCs is a difficult and complex task due to the quantum confinement effect, surfaces/interface states and surrounding matrix material [11–13], which is also different from that in its bulk counterpart.

Among of those relevant studies, the knowledge of dopant distributions and behaviors in Si NCs is the primary and necessary task to understand the doping induced physics properties and realize the controllable doping at nanoscale. Ni et al. theoretically studied the P and B distributions in the 1.4 nm Si NC embedded in SiO_2 matrix by ab-initio calculations [14,15], and found that the formation energy of P at the Si/SiO_2 interface or the surface of Si NCs was larger than that in the core. The minimum formation energy of the B dopant was obtained at the sub-interface region. Meanwhile, a lot of elemental analysis and spectroscopic methods, like secondary ion mass spectrometry (SIMS) [16,17], electron energy loss spectroscopy (EELS) [18,19] and X-ray photoelectron spectroscopy (XPS) [20,21] are performed to study the dopant distribution and concentration in Si NCs materials. In our previous studies, the depth-profile XPS spectra indicated that P and B dopants were mainly located at Si NCs inner and surfaces rather than the surrounding matrix [22]. Zhou et al. estimated the activation efficiency of B and P were 2.8–5.2% and 0.3–0.9%, respectively, by the absorption spectra [23]. However, those measurements are mainly determined the overall distribution and concentration of dopants in Si NCs sample. The precise analysis at atomic-scale are still scarce.

Atom probe tomography (APT) is a potential method to characterize

https://doi.org/10.1016/j.apsusc.2022.155260

the element information at atomic-scale [24,25]. Trad et al. have reported the influence of P dopants on the phase separation process and optical properties of Si NCs by APT measurement [26]. In this study, we fabricate P-doped and B-doped Si NCs/SiO_2 multilayers by plasma enhanced chemical vapor deposition (PECVD) system. The atomic-scale distributions and behaviors of P and B are studied by femtosecond laser-assisted APT, Raman and electron spin resonance (ESR). Results reveal that P dopants are mainly distributed at Si NCs surfaces to passivate dangling bonds, while B dopants aggregate inside Si NCs inner with a high concentration of 74.8 at. %, and lead to the damage of crystalline lattice.

2. Experiment

PECVD system equipped with the radio frequency source of 13.56 MHz was adopted to fabricate P- and B- doped Si/SiO_2 multilayers. In brief, SiH_4 gas was ionized to deposit Si sublayer on silicon wafers and quartz substrates. Meanwhile, PH_3 (1 %, H_2 dilution) and B_2H_6 (1 %, H_2 dilution) were introduced into SiH_4 plasma to act as the dopant gas. The thickness of Si sublayer was controlled by the deposition time. Then, in-situ plasma oxidation was performed in oxygen plasma atmosphere to form the thin SiO_2 sublayer. Si sublayer deposition and in-situ oxidation were alternately repeated to obtain the periodically stacked Si/SiO_2 multilayers. The deposited samples were subsequently dehydrogenated at 450 °C and annealed at 1000 °C under nitrogen gas ambient for 1 h, respectively. In this study, the P-doped and B-doped Si NCs samples have the identical nominal doping ratio (2.0 %), which is defined as molar ratio of dopant gas to SiH_4 during the deposition process.

Cross-sectional TEM (Tecnai G2 F20 electron microscope) and Raman spectrum (Horiba HR 800 Raman system, 514 nm laser) were used to characterize the microstructures of Si NCs multilayers. Element mapping and distribution were charactered by UV fermtosecond laser-assisted APT system (CAMECA LAWATAP). Low temperature (20 K) X-band ESR spectra were measured by Bruker EMX-10 with liquid-nitrogen cooled spectrometer under the center field of 3250 G.

3. Results and discussions

Fig. 1 (a) shows the Raman spectra of P-doped Si NCs/SiO_2 multilayers. For the as-deposited sample, the Raman spectrum exhibits a broad scattering packet near 470 cm^{-1} which is associated with the transverse optical mode of amorphous Si and indicate the as-deposited Si sublayers are un-crystallized [27]. After 1000 °C annealing, a sharp Raman peak around 519 cm^{-1} is observed, that is attributed to the transverse optical mode of crystallized Si phase [28]. It indicates the amorphous Si sublayers have been crystallized after 1000 °C high temperature annealing. Further, high-resolution TEM was used to study the cross-sectional microstructure of multilayers. As shown in Fig. 1 (b), the stacked structures of multilayers can be easily distinguished. The thickness of Si and SiO_2 sublayers are about 8.3 and 4.0 nm, respectively. It can be observed that the Si NCs with ellipsoid shapes are uniformly distributed in Si sublayers. The longitudinal size of Si NCs is close to the thickness of Si sublayers due to the constrained crystallization of Si/SiO_2 multilayers. In addition, the stacked structures of SiO_x ($1 \leq x \leq 2$)/SiO_2 multilayers are commonly adopted to fabricate the Si NCs embedded in matrix. However, the enriched Si atoms in adjacent SiO_x

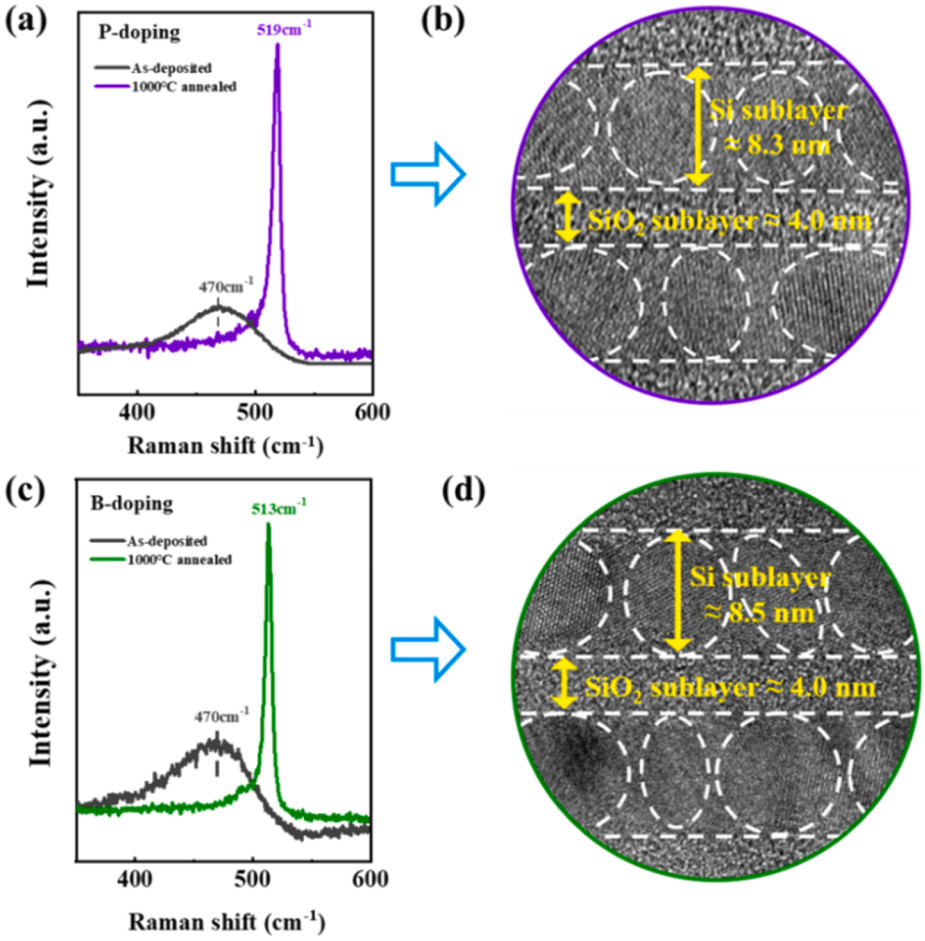

Fig. 1. (a) Raman spectra and (b) cross-sectional high-resolution TEM image of annealed P-doped Si NCs/SiO_2 multilayers; (c) Raman spectra and (d) cross-sectional high-resolution TEM image of annealed B-doped Si NCs/SiO_2 multilayers. The Raman spectra of as-deposited samples are also plotted for comparison.

sublayers are easily across SiO_2 sublayers to form large Si NCs under thermal annealing [29], which can break the constrained crystallization effect of multilayers. Fig. 1 (c) also exhibits the Raman spectra of B-doped Si NCs/SiO_2 multilayers. After annealing, the Si-Si bonds related Raman peak accompanying with an obvious redshift is detected. The redshift has also observed in the B-doped Si nanowires, which is mainly attributed to the B-doping induced tense stress in films. Meanwhile, a weak and broad Raman peak around 628 cm^{-1} is observed in Fig. S1, which is believed arising from the Raman scattering related to the B-Si local vibration signals and indicate the B atoms are doped in substitutional sites of the Si NCs [30]. As shown in Fig. 1 (d), the sizes of B-doped Si NCs within the thickness of the Si sublayers are also strictly obeyed.

To investigate more into details of the element distribution, the APT measurements are performed. Fig. 2 (a) exhibits the elemental mapping of Si and O compositions for as-deposited P-doped multilayers. Alternately stacked structure is clearly observed. The aggregation regions of O atoms (in green color) are corresponding to the SiO_2 sublayers with the thickness near 4.0 nm, and the gathered regions of Si atoms are the Si sublayers with the thickness about 8.3 nm. Indeed, the stacked structure and thickness of sublayers from APT measurement are in good accord with the high-resolution TEM results. Further, the concentration profiles of Si and O compositions for as-deposited P-doped multilayers are shown in Fig. 2 (b). The interfaces between Si and SiO_2 sublayers can be visualized identified by the intersections of Si and O concentration curves, where the values of Si and O concentrations are both 50.0 at. %, respectively. For convenience, the position of one of the interfaces is selected as the origin of the horizontal axis in the concentration profiles. The negative and positive axis directions point towards the SiO_2 or Si (or Si NCs) sublayers. As shown in the profiles, the distance dependent Si and O concentrations exhibit the periodic variations associating with the structural characteristics of multilayers. From the APT results, the averaged Si concentration in Si sublayers reach to 92.2 at. %. For the SiO_2 sublayers, the Si and O concentrations are 33.1 and 66.3 at. % respectively, which meets the stoichiometric ratio of SiO_2.

Fig. 2 (c) shows the APT elemental mapping of annealed P-doped Si NCs multilayers, and the Si and O compositions are separately reconstructed for more intuitive observation on the structures and elements distributions. It is found that the periodically stacked structures of multilayers and the thickness of sublayers keep unchanged after 1000 °C annealing for 1 h. The interfaces between Si NCs and SiO_2 sublayers are smooth and abrupt without the diffusion of O atoms into Si NCs sublayers. In Fig. 2 (d), the Si and O concentration profiles also exhibit structure related periodic variations. The Si contents in Si NCs sublayers reach to as high as 97.8 at. %, and the Si and O concentrations in SiO_2 sublayers also keep at the stoichiometric ratios.

Further, the dopant distributions in the multilayers are focally studied. Fig. 3 exhibits the concentration profiles of P dopants for the unannealed and annealed P-doped Si NCs/SiO_2 multilayers. For the as-deposited sample, it is found that the P dopants are randomly distributed in Si sublayers and the averaged concentration is near 0.64 at. %. Meanwhile, few P dopants are located at the SiO_2 sublayers with a low concentration near 0.25 at. %, which is because the SiO_2 sublayers were fabricated by in-situ oxidation of Si sublayers. After annealing, the P dopants in Si sublayers are redistributed. First, P dopants are mainly gathered at the interface regions i.e. the surfaces of Si NCs with a high concentration near 1.36 at. %, and then decrease rapidly towards both side directions, i.e. SiO_2 and Si NCs sublayers. Then, the P concentrations in SiO_2 sublayers keep almost unchanged before and after annealing. It is attributed to the stable stoichiometric ratios and microstructure of SiO_2 sublayers. Moreover, the averaged P concentration inside Si NCs sublayers decrease to 0.45 at. %, which is lower than that of as-deposited Si sublayers. Hence, the P dopants gathered at interfaces are mainly migrated from the diffusion of P dopants, which are initially distributed in Si sublayers.

The redistributions of P dopants in Si sublayers are attributed to the formation of Si NCs under high temperature annealing. APT results have indicated that P dopants prefer to locate at the surfaces regions of Si NCs, while part of them are incorporated into Si NCs inner. The distribution of

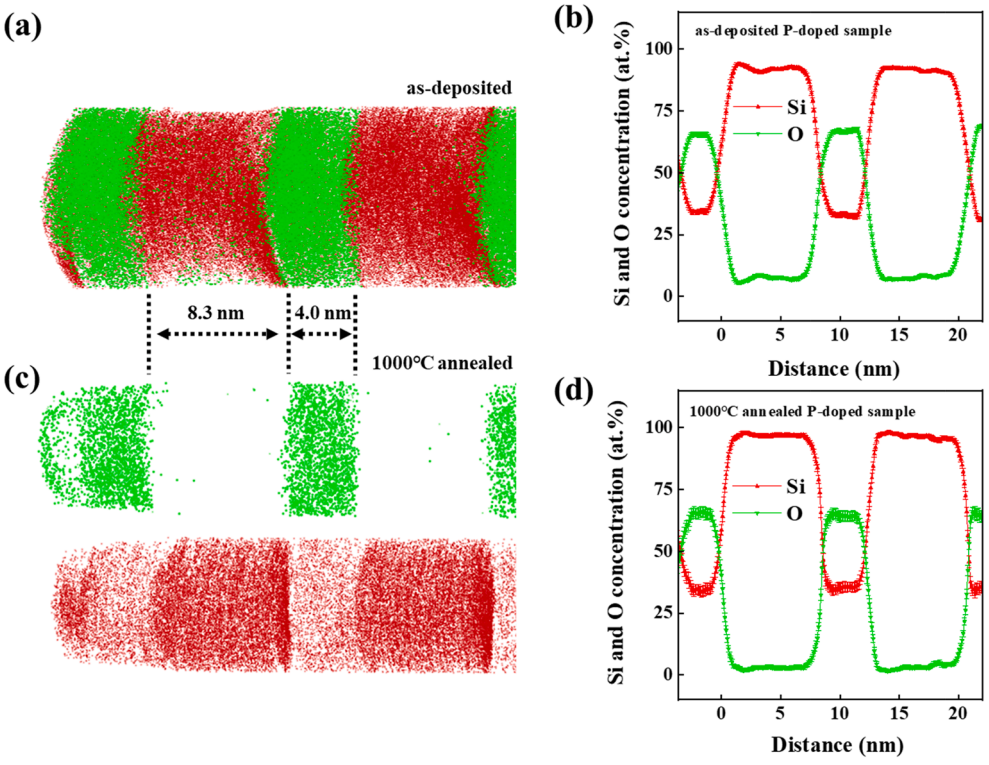

Fig. 2. (a) APT elemental mapping and (b) concentration profiles of Si and O compositions for as-deposited P-doped multilayers; (c) APT elemental mapping and (d) concentration profiles of Si and O compositions for annealed P-doped multilayers. Si and O are plotted in red and green color, respectively. (For interpretation of the references to color in this figure legend, the reader is referred to the web version of this article.)

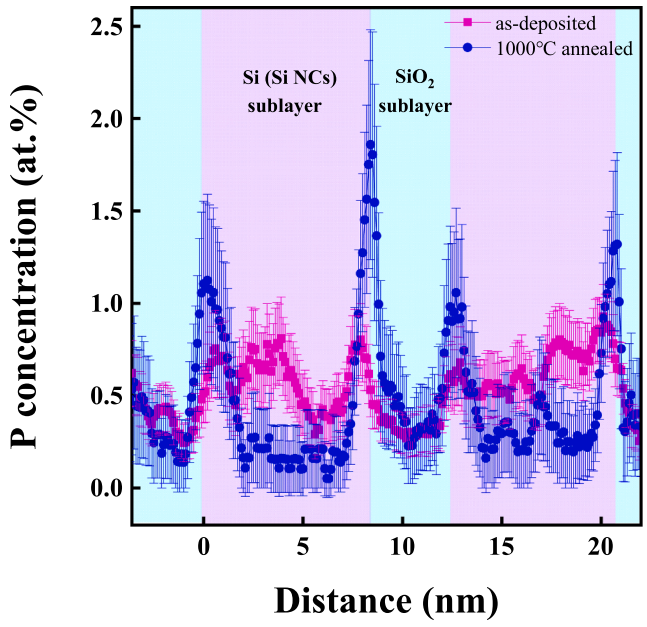

Fig. 3. P concentration profiles of unannealed (in pink color) and annealed (in blue color) P-doped Si NCs multilayers. The backgrounds in purple and turquoise colors represent the Si (Si NCs) and SiO_2 sublayers, respectively. (For interpretation of the references to color in this figure legend, the reader is referred to the web version of this article.)

P in Si NCs can be mainly attributed to two reasons, (i) during the growth process, Si NCs tend to expel the dopants to their surfaces to keep the stability of crystal structures, which is similar with the reported self-purifications effects in Mn-doped CdSe nanocrystals [31]; (ii) P dopants have the lowest formation energy when locating at the surface sites than the inner sites of Si NCs [15]. As a result, the P dopants exhibit higher distribution concentration at the surfaces regions than that of Si NCs inner. Moreover, it is found the P-doped Si NCs sample is n-type with the electron concentration of $1.80 \times 10^{20}/cm^3$ [9]. The carrier concentrations stand for the electrically activated dopants at lattice sites of Si NCs. Using the estimated atomic density of the Si NCs (6.70×10^{22} atoms/cm^3), the calculated activation concentration of P dopants in Si NCs is 0.27 at. %, which is more than half of the value measured by APT. It reveals that most of P dopants in Si NCs sublayers are substitutionally incorporated into Si NCs inner.

The distribution of B dopants in Si NCs multilayers is also studied. As shown in Fig. 4 (a), the distribution of B dopants in Si NCs sublayers is more complex. Part of B dopants is gathered at the interfaces between SiO_2 and Si NCs sublayers, which is similar with the distribution of P dopants. Besides, the B dopants at the interface regions diffuse into SiO_2 sublayers to some extent. In order to gain more insight into the B dopant distribution at interfaces regions i.e. the surfaces of Si NCs, the element concentration of section I and II in the mapping image is studied and shown in Fig. 4 (b) and (c), respectively. It is found that the B concentration at the surfaces of Si NCs can reach as high as 40.0 at. %, and the thickness of enriched B region is about 2.0 nm which is like the shells covering on the Si NCs surfaces. In the optical study of B-doped Si NCs multilayers, we have found that the optical emission originated from the Si-oxide centers surrounding Si NCs surfaces are gradually quenching with the increase of B-doping ratios [32]. The B dopant shells can cause the segregation of Si and O atoms at the interfaces and suppress the formation of Si-oxide emission centers on Si NCs surfaces, which may be responsible for the quenching of Si-oxide surface states related optical emission. As reported, B dopants are easily bonded with the surrounding O atoms due to the large electronegativity differences between B and O atoms [14]. It may result in the diffusion of B dopants into SiO_2 sublayers as shown in the mapping image and concentration profiles.

More interesting, it is found that a lot of B dopants are also aggregated near the middle of Si NCs sublayers, which is different from P

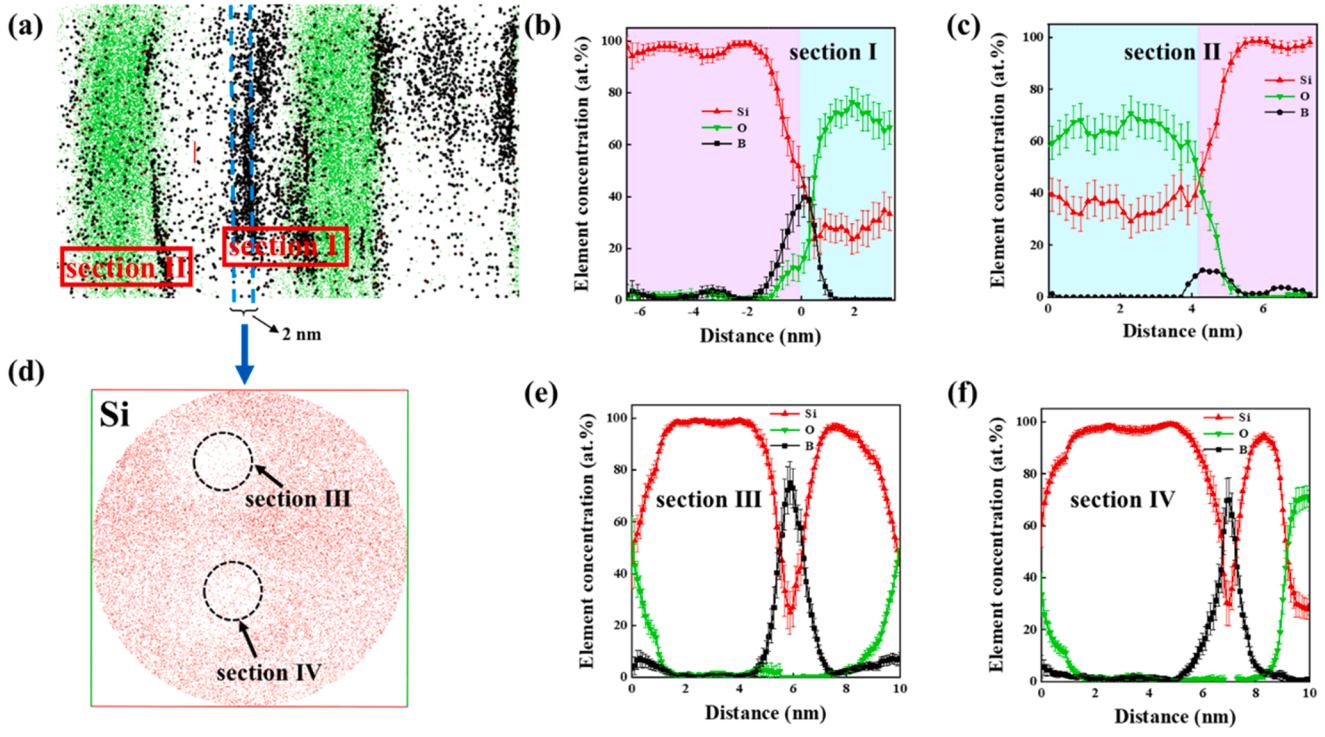

Fig. 4. (a) APT elemental mapping of O and B compositions for annealed B-doped Si NCs multilayers; (b) and (c) are the element concentration profiles of the section I and II; (d) slice view of Si atoms taken from the B aggregation region in Si NCs sublayer; (e) and (f) are the element concentration profiles of the section III and IV, respectively. Si, O and B are plotted in red, green and black colors, respectively. (For interpretation of the references to color in this figure legend, the reader is referred to the web version of this article.)

dopants. The slice analysis taken from the B aggregation region is performed to study the element composition, the results of Si atoms are shown in Fig. 4 (c). In the slice image, the obvious aggregation of Si atoms which usually standing for the Si NCs is not appeared. Meanwhile, B dopants are enriched in the blank area of Si atoms, like section III and IV. Fig. 4 (e) and (f) show the element concentration profiles of the section III and IV, respectively. It is found the positions with the maximal B concentration appear near the middle of Si sublayers, and the value of B concentration can reach as high as 74.8 at. %. The high B concentration in Si NCs/SiO_2 multilayers is similar with the results of B hyper-doped Si NCs fabricated by laser induced reactor under nonequilibrium conditions [8]. For the as-deposited B-doped Si/SiO_2 multilayers, the B dopants are initially uniformly distributed in the amorphous silicon sublayers. During the high temperature annealing, the doping process of B dopants is simultaneously accompanied with the growth process of Si NCs. Besides the effect of thermodynamics, the B dopants are also subject to the collisions from the surrounding Si atoms with large atomic mass, which may lead to the B dopants also in a non– or sub-thermodynamic equilibrium state. However, it is difficult to pinpoint the location of this kind B-aggregations in Si NCs due to the two main possibilities, (i) B-aggregation may locates at the surfaces of Si NCs, which means the predesigned Si NC with size near 8.0 nm in the Si layers are divided into two smaller Si NCs by B-aggregation; (ii) B-aggregation locates at the Si NCs inner and act as part of nanocrystals.

Further, the low temperature (20 K) ESR measurement was performed to study the dopants behaviors in Si NCs multilayers. As shown in Fig. 5, a strong ESR signal with g = 2.005 is detected for both 450 °C dehydrogenated P-doped and B-doped multilayers, which can be assigned to the Si dangling bonds [33]. The Si dangling bonds are generated due to the effusion of H from the Si/SiO_2 multilayers after 450 °C thermally annealing. In our previous studies, the Si dangling bonds were still existed on the surfaces of un-doped Si NCs. After P-doping, the ESR signal of Si dangling bonds disappeared. It can be attributed to the passivation effect of P dopants locating at the surface regions of Si NCs [33]. Mimura et al. have also theoretically reported that P can passivate defects such as Si dangling bonds at the Si/SiO_2 interfaces when Si NCs embedded in SiO_2 were doped with P dopants [34]. Moreover, a strong signal of conductor electrons is detected with a g value of 1.998. It is attributed to part of P dopants are substitutionally incorporated into Si NCs lattice sites to provide free electrons [9,10].

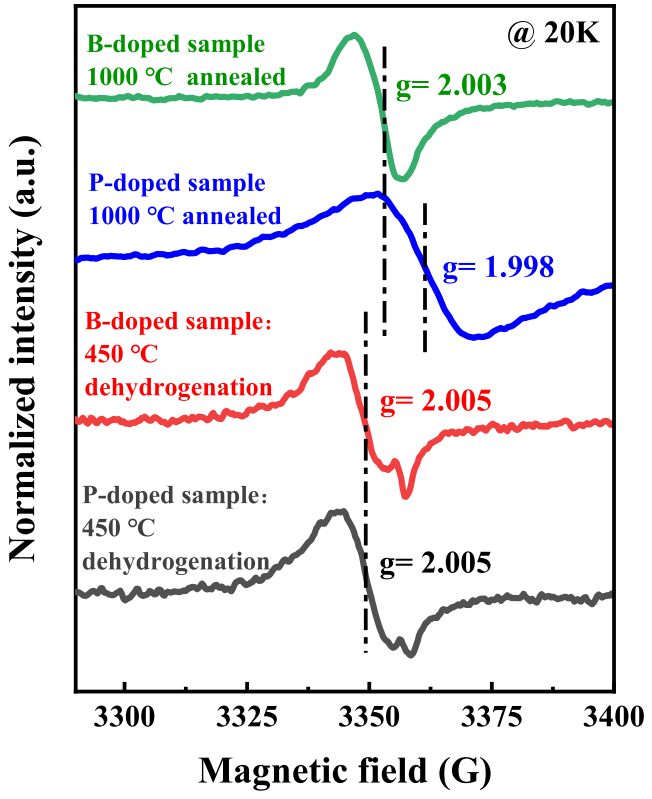

Fig. 5. Low temperature (20 K) ESR spectra of P-doped and B-doped Si NCs/SiO2 multilayers.

After B-doping, the ESR signal of Si dangling bonds on Si NCs surfaces is also disappeared. APT results have revealed that the B dopants locate at Si NCs surfaces and form the dopant-shell covering on the Si NCs surfaces. The shell of B dopants can modify the surface states, such as Si dangling bonds. Veettil et al. have reported the B dopants can passivate the dangling bonds of self-assembled Si NCs [35]. Sugimoto et al. also found the P/B co-doped Si NCs had an amorphous shell mainly made from B, and the shell induced negative potential on the surface and made co-doped Si NCs dispersible in water [36]. Hence, the disappear of Si dangling bonds of B-doped Si NCs is attributed to the passivation effect of B dopants locating on the Si NCs surfaces regions. The strong ESR signal with g = 2.003 in B-doped Si NCs is originated from the Si vacancy, which is caused by the damage of Si crystalline lattice. In the study of hyper P-doped Si NCs, similar damage of crystalline lattice was also observed due to the large amount of intensively moving P atoms [33]. For our B-doped Si NCs, the Si vacancy is mainly due to the high incorporation concentration of B in Si NCs inner. In our opinion, the B-aggregations observed at the middle region of Si sublayers may locate inside the Si NCs rather than on the surfaces of two small Si NCs. Comparing with P and B dopants, both P and B are preferred to distribute on the surface of Si NCs, which is mainly due to the self-purification effect during the doping process. Moreover, a large number of defects on the surface of Si NCs generally have low formation energy for dopants, which has been confirmed by ESR results. Ni et al. and Rohani et al. have reported B dopants are easier than P to achieve hyper-doping in Si NCs [8,37]. Ni et al. believe that the collision between Si NCs and B or P atoms is critical to the understanding on the differences in the doping efficiency and dopant distribution between B and P. The collision frequency for B with small atomic mass is larger than that for P, which result in the high doping efficiency of B. In addition to the easily forced collision of B dopants during the Si NCs crystallization, the smaller binding energy of the B-B bond may be also an important factor for the formations of B-aggregations in Si NCs inner and the B-shells on the Si NC surfaces [14].

4. Conclusion

P-doped and B-doped Si/SiO_2 multilayers are fabricate by PECVD system. Si NCs with uniform size distribution are obtained due to the constrained crystallization effect of hetero-structured multilayers. APT mapping reveals that the multilayers have the stable microstructure even annealed under 1000 °C high temperature, and the P dopants in Si sublayers are redistributed accompanying with the formation of Si NCs. For the as-deposited sample, P dopants are randomly distributed in Si sublayers with average concentration near 0.64 at. %. After annealing, the P dopants gather at the surface regions with the concentration reaching to 1.36 at. %. ESR results indicate that the dangling bonds on Si NCs surface are passivated by P dopants, and part of P are also incorporated into Si NCs lattice sites to provide free electrons. In contrast, B dopants inside Si NCs are gathered as aggregations to damage the crystalline lattice. Meanwhile, the B dopants form a dopant-shell on Si NCs surface with the thickness near 2 nm. The B dopant-shell can modify the surfaces states of Si NCs, which may broad the application of Si NCs in optical materials and water-soluble biomonitoring.

CRediT authorship contribution statement

Dongke Li: Investigation, Funding acquisition, Data curation, Formal analysis, Writing - original draft, Writing - review & editing.

Jiaming Chen: Investigation. **Zhaoguo Xue:** Investigation. **Teng Sun:** Investigation. **Junnan Han:** Investigation. **Wanghua Chen:** Funding acquisition, Formal analysis, Writing - original draft. **Etienne Talbot:** Investigation, Funding acquisition. **Rémi Demoulin:** Investigation, Funding acquisition. **Jun Xu:** Funding acquisition, Supervision, Writing - original draft, Writing - review & editing.

Declaration of Competing Interest

The authors declare that they have no known competing financial interests or personal relationships that could have appeared to influence the work reported in this paper.

Data availability

No data was used for the research described in the article.

Acknowledgement

This work is supported by National Key R&D program of China (2018YFB2200101); NSFC (62004078, 61921005); NSF of Jiangsu Province (BK20201073); NSF of Jiangsu Higher Education Institutions (20KJB510017); Natural Science Foundation of Ningbo (2021J068); ANR DONNA (ANR-18-CE09-0034). Low temperature ESR test was performed on the Steady High Magnetic Field Facilities, High Magnetic Field Laboratory, CAS.

Appendix A. Supplementary data

Supplementary data to this article can be found online at https://doi.org/10.1016/j.apsusc.2022.155260.

References

[1] Z.Y. Ni, S. Zhou, S.Y. Zhao, W.B. Peng, D.R. Yang, X.D. Pi, Silicon nanocrystals: unfading silicon materials for optoelectronics, Mater. Sci. Eng. R-Rep. 138 (2019) 85–117.
[2] F. Priolo, T. Gregorkiewicz, M. Galli, T.F. Krauss, Silicon nanostructures for photonics and photovoltaics, Nat. Nanotechnol. 9 (2014) 19–32.
[3] D. Liang, J.E. Bowers, Recent progress in lasers on silicon, Nat. Photonics 4 (2010) 511–517.
[4] H. Hao, Y. Zhao, T. Song, X. Wang, C. Li, W. Li, W. Shen, Enhancement in external quantum efficiency of light-emitting diode based on colloidal silicon nanocrystals, Nanotechnology 32 (2021), 505611.
[5] Y.Q. Cao, P. Zhu, D.K. Li, X.H. Zeng, D. Shan, Size-Dependent and Enhanced Photovoltaic Performance of Solar Cells Based on Si Quantum Dots, Energies 13 (2020) 4845.
[6] L. Yin, W. Huang, R. Xiao, W. Peng, Y. Zhu, Y. Zhang, X. Pi, D. Yang, Optically Stimulated Synaptic Devices Based on the Hybrid Structure of Silicon Nanomembrane and Perovskite, Nano Lett. 20 (2020) 3378–3387.
[7] D. Li, J. Chen, T. Sun, Y. Zhang, J. Xu, W. Li, K. Chen, Enhanced subband light emission from Si quantum dots/SiO_2 multilayers via phosphorus and boron co-doping, Opt. Express 30 (2022) 12308–12315.
[8] P. Rohani, S. Banerjee, S. Sharifi-Asl, M. Malekzadeh, R. Shahbazian-Yassar, S.J. L. Billinge, M.T. Swihart, Synthesis and Properties of Plasmonic Boron-Hyperdoped Silicon Nanoparticles, Adv. Funct. Mater. 29 (2019) 1807788.
[9] D. Li, Y. Jiang, P. Zhang, D. Shan, J. Xu, W. Li, K. Chen, The phosphorus and boron co-doping behaviors at nanoscale in Si nanocrystals/SiO_2 multilayers, Appl. Phys. Lett. 110 (2017), 233105.
[10] D. Li, Y. Jiang, J. Liu, P. Zhang, J. Xu, W. Li, K. Chen, Modulation of surface states by phosphorus to improve the optical properties of ultra-small Si nanocrystals, Nanotechnology 28 (2017), 475704.
[11] D. Li, J. Xu, P. Zhang, Y. Jiang, K. Chen, Doping effect in Si nanocrystals, Journal of Physics D-Applied, Physics 51 (2018), 233002.
[12] I. Marri, E. Degoli, S. Ossicini, Doped and codoped silicon nanocrystals: The role of surfaces and interfaces, Prog. Surf. Sci. 92 (2017) 375–408.
[13] B.L. Oliva-Chatelain, T.M. Ticich, A.R. Barron, Doping silicon nanocrystals and quantum dots, Nanoscale 8 (2016) 1733–1745.
[14] Z. Ni, X. Pi, S. Cottenier, D. Yang, Density functional theory study on the B doping and B/P codoping of Si nanocrystals embedded in SiO_2, Physical Review B 95 (2017), 159905.
[15] Z.Y. Ni, X.D. Pi, D.R. Yang, Doping Si nanocrystals embedded in SiO_2 with P in the framework of density functional theory, Physical Review B 89 (2014), 035312.
[16] X.J. Hao, E.C. Cho, G. Scarder, Y.S. Shen, E. Bellet-Amalric, D. Bellet, G. Conibeer, M.A. Green, Phosphorus-doped silicon quantum dots for all-silicon quantum dot tandem solar cells, Sol. Energy Mater. Sol. Cells 93 (2009) 1524–1530.
[17] X.J. Hao, E.C. Cho, C. Flynn, Y.S. Shen, S.C. Park, G. Conibeer, M.A. Green, Synthesis and characterization of boron-doped Si quantum dots for all-Si quantum dot tandem solar cells, Sol. Energy Mater. Sol. Cells 93 (2009) 273–279.
[18] K. Sato, K. Niino, N. Fukata, K. Hirakuri, Y. Yamauchi, The synthesis and structural characterization of boron-doped silicon-nanocrystals with enhanced electroconductivity, Nanotechnology 20 (2009), 365207.
[19] K. Sato, N. Fukata, K. Hirakuri, Doping and characterization of boron atoms in nanocrystalline silicon particles, Appl. Phys. Lett. 94 (2009), 161902.
[20] M. Perego, C. Bonafos, M. Fanciulli, Phosphorus doping of ultra-small silicon nanocrystals, Nanotechnology 21 (2010), 025602.
[21] N. Garcia-Castello, S. Illera, J.D. Prades, S. Ossicini, A. Cirera, R. Guerra, Energetics and carrier transport in doped Si/SiO2 quantum dots, Nanoscale 7 (2015) 12564–12571.
[22] J. Chen, D. Li, Y. Zhang, Y. Jiang, J. Xu, K. Chen, Comparative study on P and B doped nano-crystalline Si multilayers, Appl. Surf. Sci. 529 (2020), 146971.
[23] S. Zhou, X.D. Pi, Z.Y. Ni, Y. Ding, Y.Y. Jiang, C.H. Jin, C. Delerue, D.R. Yang, T. Nozaki, Comparative Study on the Localized Surface Plasmon Resonance of Boron- and Phosphorus-Doped Silicon Nanocrystals, ACS Nano 9 (2015) 378–386.
[24] W. Chen, L. Yu, S. Misra, Z. Fan, P. Pareige, G. Patriarche, S. Bouchoule, P. Roca i Cabarrocas, Incorporation and redistribution of impurities into silicon nanowires during metal-particle-assisted growth, Nature Communitions 5 (2014) 4134.
[25] D. Konig, S. Gutsch, H. Gnaser, M. Wahl, M. Kopnarski, J. Gottlicher, R. Steininger, M. Zacharias, D. Hiller, Location and Electronic Nature of Phosphorus in the Si Nanocrystal–SiO2 System, Sci. Rep. 5 (2015) 9702.
[26] F. Trad, A.E. Giba, X. Devaux, M. Stoffel, D. Zhigunov, A. Bouche, S. Geiskopf, R. Demoulin, P. Pareige, E. Talbot, M. Vergnat, H. Rinnert, Influence of phosphorus on the growth and the photoluminescence properties of Si-NCs formed in P-doped SiO/SiO2 multilayers, Nanoscale 13 (2021) 19617–19625.
[27] L. Khriachtchev, S. Novikov, J. Lahtinen, Thermal annealing of Si/SiO2 materials: Modification of structural and photoluminescence emission properties, J. Appl. Phys. 92 (2002) 5856–5862.
[28] T. Nikitin, S. Novikov, L. Khriachtchev, Giant Raman gain in annealed silicon-rich silicon oxide films: Measurements at 785 nm, Appl. Phys. Lett. 103 (2013), 151110.
[29] R. Limpens, A. Lesage, M. Fujii, T. Gregorkiewicz, Size confinement of Si nanocrystals in multinanolayer structures, Scientic Reports 5 (2015) 17289.
[30] N. Fukata, Impurity Doping in Silicon Nanowires, Adv. Mater. 21 (2009) 2829–2832.
[31] G.M. Dalpian, J.R. Chelikowsky, Self-purification in semiconductor nanocrystals, Phys. Rev. Lett. 96 (2006), 226802.
[32] J. Chen, D. Li, T. Sun, J. Han, L. Wang, Y. Zhang, J. Xu, K. Chen, Study on luminescence quenching of ultra-small silicon nanocrystals due to boron doping, Optical Materials Express 12 (2022) 4096–4103.
[33] P. Lu, W. Mu, J. Xu, X. Zhang, W. Zhang, W. Li, L. Xu, K. Chen, Phosphorus Doping in Si Nanocrystals/SiO2 multilayers and Light Emission with Wavelength compatible for Optical Telecommunication, Sci. Rep. 6 (2016) 22888.
[34] A. Mimura, M. Fujii, S. Hayashi, D. Kovalev, F. Koch, Photoluminescence and free-electron absorption in heavily phosphorus-doped Si nanocrystals, Phys. Rev. B 62 (2000) 12625–12627.
[35] B.P. Veettil, L.F. Wu, X.G. Jia, Z.Y. Lin, T. Zhang, T. Yang, C. Johnson, D. McCamey, G. Conibeer, I. Perez-Wurfl, Passivation effects in B doped self-assembled Si nanocrystals, Appl. Phys. Lett. 105 (2014), 222108.
[36] H. Sugimoto, H. Zhou, M. Takada, J. Fushimi, M. Fujii, Visible-light driven photocatalytic hydrogen generation by water-soluble all-inorganic core-shell silicon quantum dots, J. Mater. Chem. A 8 (2020) 15789–15794.
[37] S. Zhou, X.D. Pi, Z.Y. Ni, Q.B. Luan, Y.Y. Jiang, C.H. Jin, T. Nozaki, D.R. Yang, Boron- and Phosphorus-Hyperdoped Silicon Nanocrystals, Part. Part. Syst. Char. 32 (2015) 213–221.